JACS
JOURNAL OF THE AMERICAN CHEMICAL SOCIETY

Article

pubs.acs.org/JACS

High-Quality Metal–Organic Framework Ultrathin Films for Electronically Active Interfaces

Víctor Rubio-Giménez,[†] Sergio Tatay,[†] Florence Volatron,[†] Francisco J. Martínez-Casado,[‡] Carlos Martí-Gastaldo,*[,†] and Eugenio Coronado*[,†]

[†]Instituto de Ciencia Molecular, Universitat de València, Catedrático José Beltrán 2, 46980 Paterna, Spain

[‡]MAX IV Laboratory, Lund University, Fotongatan 2, 225 94 Lund, Sweden

Supporting Information

ABSTRACT: Currently available methodologies arguably lack the exquisite control required for producing metal–organic framework (MOF) thin films of sufficient quality for electronic applications. By directing MOF transfer with self-assembled monolayers (SAMs), we achieve very smooth, homogeneous, highly oriented, ultrathin films across millimeter-scale areas that display moderate conductivity likely due to electron hopping. Here, the SAM is key for directing the transfer thereby enlarging the number and nature of the substrates of choice. We have exploited this versatility to evolve from deposition onto standard Si and Au to nonconventional substrates such as ferromagnetic Permalloy. We believe that this strategy might be useful for the integration of MOFs as active interfaces in electronic devices.

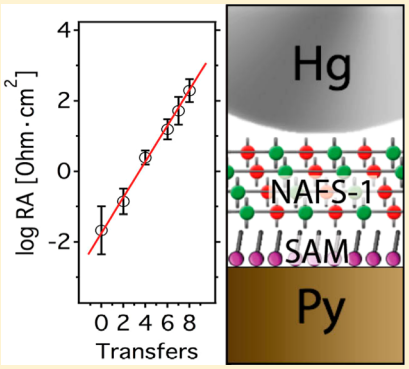

INTRODUCTION

The past decade has witnessed a spectacular development of organic-based electronic devices. Although digital displays based on organic light-emitting diodes (OLEDs) are already commercially available,[1] molecular photovoltaic devices have recently emerged as feasible competitors of silicon on the basis of the very high efficiencies reported: up to 20% with a fivefold increase in the last three years.[2] Molecular alternatives also offer low-cost processing and easy manipulation of performance/function by the enormous number of molecules of choice. One of the main characteristics of these devices is their hybrid nature because they combine organic active materials with inorganic electrodes. Most properties of these devices are crucially determined by their hybrid interfaces so that the ability to tailor the degree of interaction between organic and inorganic materials generally impacts the electronic properties of the composite materials and the functioning of the entire device. In fact, the performance of these devices is often limited by the electrical barrier at the interface and by the conductivity mismatch between the inorganic metal and the organic semiconductor. Active manipulation of the organic/inorganic interface is key to overcome these limitations. In this context, an attractive approach is that of inserting an interfacial molecular layer in between the inorganic electrode and the organic active layer. Its role will be that of connecting the materials at both sides of the molecular interface. This approach has been extensively used in the fabrication of OLEDs and both electron- and hole-injection layers are often used to improve the device performance.[3] Another area in which the interface engineering is important is molecular spin-electronics (or spintronics).[4] Here the design of active interfaces is even more important because one needs to control not only the charge transfer but also the spin transfer across the interface. However, this area is quite new, and most of the efforts have been focused on studying the spin injection and transport processes in the spintronic device whereas active manipulation of the hybrid interface remains almost unexplored.[5,6] In fact, these attempts have been so far limited to deposit self-assembled monolayers (SAMs) of dipolar molecules on the ferromagnetic electrode.[6] In this work, we aim to go one step beyond current interface engineering by controlling the deposition of ultrathin films of metal–organic frameworks (MOFs) on a ferromagnetic electrode.

MOFs are hybrid materials built from the interconnection of metal ions or clusters and organic linkers, in which the multiple combination of organic/inorganic blocks renders periodic structures with unparalleled structural and functional diversity.[7] Owing to the framework's porosity, MOFs are interesting materials for gas storage[8] and/or separation,[9] catalysis,[10] sensing,[11] or ionic transport.[12] Although most studies available concern bulk solids, exploitation of MOFs' intrinsic features by integrating them as thin films in solid supports poses a key challenge with important technological implications.[13] MOF thin films can be divided in two general groups: (i) polycrystalline films of micrometer-scale thickness that are generally grown by seeding methods with poor control over orientation of the crystals and (ii) ultrathin (nanometer-scale)

Received: September 17, 2015
Published: February 5, 2016

DOI: 10.1021/jacs.5b09784
J. Am. Chem. Soc. 2016, 138, 2576–2584

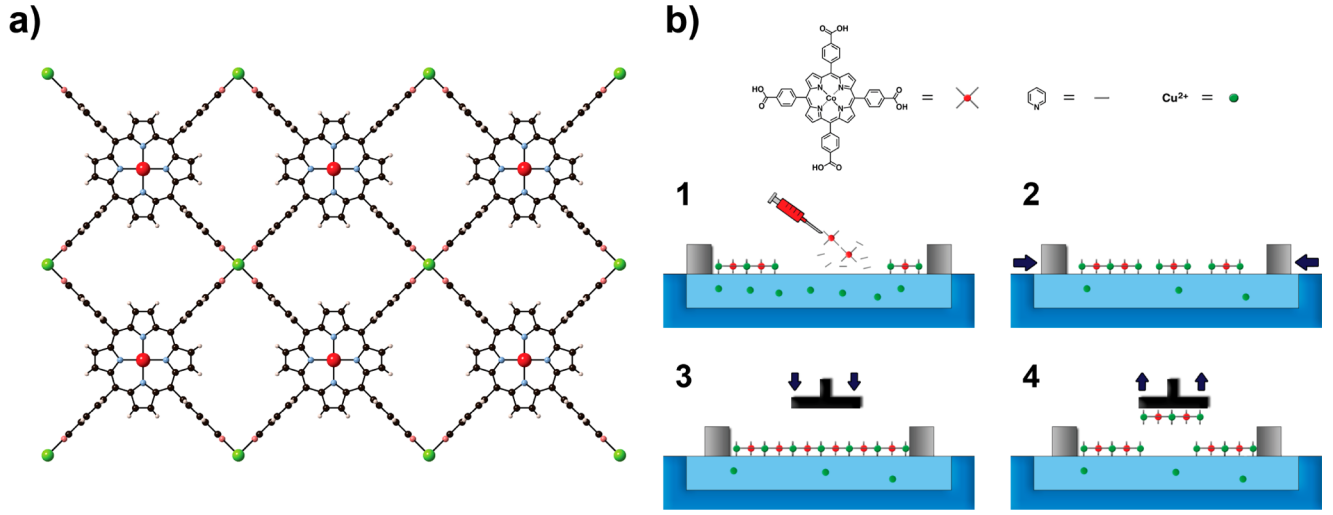

Figure 1. NAFS-1 structure and Langmuir–Blodgett (LB) transfer process. (a) Structure of a single layer of NAFS-1 viewed along the *c* axis. The pyridine (py) molecules, which are axially coordinated to Co(II) and Cu(II) metal centers to interconnect neighboring nanosheets via $\pi-\pi$ stacking, have been omitted for clarity. Color code: Co, red; Cu, green; O, salmon; N, blue; C, black; and H, gray. (b) Scheme for nanosheet formation, compression, and transfer to the substrate in a LB trough. (1) Spreading of the molecular components (CoTCPP and py) on the Cu(II) aqueous subphase causes immediate formation of inhomogeneously distributed MOF arrays (2) After barrier pressing, the arrays are gathered to a smaller area, raising surface pressure. (3) When a continuous monolayer has been formed, the substrate is horizontally approached to the surface until they make contact. (4) Finally, the substrate is lifted, and the floating monolayer is transferred to the substrate.

films grown by layer-by-layer (LbL) sequential deposition of MOF layers. This last method is referred to as liquid-phase epitaxy, and the resulting surface MOFs (SURMOFs) feature good orientation and very low roughness.[14] This synthesis knowledge has allowed development of a first generation of MOF-based devices of interest as separation membranes, catalytic coatings, or optical/chemical sensors that exploit almost exclusively the framework's porosity as active function.[15]

There is an increasing interest in developing an advanced generation of electronic and optoelectronic devices that make use of electronically active MOFs besides exploiting their porosity.[16] However, this type of applications is expected to be much more demanding with the quality of the films required for device integration because it relies on the fabrication of MOF films with fine control over morphology, density, crystallinity, roughness, and orientation; these are all severe requirements for device performance. Investigation of the electrical conductivity of MOF thin films at the nanoscale (<100 nm) still remains a challenge likely due to the difficulties in producing films of the required quality. Hence, development of chemical strategies that enable processing of MOFs as nanometric thick films with fine control over these features poses a key challenge with important technological implications.

We introduce a nonconventional strategy that relies on sequential transfer of 2D preassembled MOF nanosheets to SAM-functionalized substrates in order to produce high-quality MOF ultrathin films. LbL deposition allows for better control over the quality of the film because it minimizes the problems linked to uncontrolled crystal growth and substrate-directed crystallization processes, which generally lead to grain segregation for poor morphology. Our approach is only valid for layered MOFs featuring weak interlayer interactions because they need to be replicated on the substrate by sequential transfer of their constituting layers. This is why we have chosen as a model system NAFS-1,[17] a layered MOF built from the sequential stacking of 2D networks of Co(II) tetracarboxylate porphyrin units interconnected by Cu(II) ions (Figure 1a). In contrast with previous methodologies, SAM-assisted transfer enables the fabrication of homogeneous, highly oriented, ultrathin films across millimeter-scale areas, regardless of the substrate. Our Hg-drop electrode junction studies are indicative of moderate electrical conductivity in ultrathin MOF films for the first time and suggest a hopping mechanism as the most likely origin.

EXPERIMENTAL SECTION

Synthesis. *Materials and Reagents.* 5,10,15,20-Tetrakis(4-carboxyphenyl)porphyrinato-cobalt(II) (CoTCPP) (Porphyrin Systems, 97%), pyridine (py) (Sigma-Aldrich, ≥ 99%), $Cu(NO_3)_2{\cdot}3H_2O$ (Sigma-Aldrich, ≥ 99%), 1-dodecylphosphonic acid (C12P) (Alfa Aesar, 95%), and 1-dodecanethiol (C12S) (Sigma-Aldrich, ≥ 98%) were used as received without further purification. Solvents (HPLC-grade) were purchased from Scharlab S.L. Ultrapure Milli-Q water with a resistivity higher than 18 MΩ·cm was used when required.

Substrate Preparation. Prior to evaporation of permalloy (Py), glass substrates were soaked in a freshly prepared solution of $H_2O_2/NH_4OH/H_2O$ (1:1:2) and sonicated for 10 min. This treatment was repeated three times. Next, they were rinsed with Milli-Q water, sonicated 5 min in Milli-Q water twice, and dried under a N_2 stream. The Py layer was then evaporated in a Edwars Auto 500 thermal evaporator in a tungsten basket coated with Al_2O_3 placed inside a nitrogen glovebox. Base pressure was 2×10^{-6} mbar, and evaporation rate 0.02 nm s^{-1}. 15 nm Py was the preferred thickness except for infrared spectroscopy studies where 150 nm were used. For SAM functionalization, Py substrates were previously activated via H_2 plasma treatment (MiniPCFlecto, Plasma Technology) and then immersed in a 2 mM 2-propanol solution of C12P for 12 h. Next, substrates were rinsed with fresh 2-propanol, dried under a N_2 stream, and heated at 60 °C for 5 min. For Au SAM functionalization, substrates were previously dipped in a freshly prepared solution of H_2O_2/H_2SO_4 (1:1), rinsed with Milli-Q water and ethanol, and then immersed in a 1 mM ethanol solution of C12S for 12 h. Next, substrates were rinsed with fresh ethanol and dried under a N_2 stream. SAM quality was evaluated by dynamic water contact angle (CA) measurements.

DOI: 10.1021/jacs.5b09784
J. Am. Chem. Soc. 2016, 138, 2576–2584

Film Preparation. We used freshly prepared solutions of CoTCPP (0.04 mM) and py (1 mM) in chloroform/methanol solvent (3:1, v/v) for all Langmuir−Blodgett (LB) experiments. A KSV Nima polytetrafluoroethylene (PTFE)-coated Langmuir minitrough (8720 mm^2) was thoroughly cleaned with methanol and dichloromethane using surfactant-free wipes before filling it with 1 mM $Cu(NO_3)_2 \cdot 3H_2O$ aqueous solution as a subphase. Next, the surface of the subphase was carefully cleaned by mild surface-touch vacuuming. The CoTCPP-py solution (150 μL) was carefully spread drop-by-drop onto the subphase using a Hamilton microsyringe. Surface pressure (π) was monitored using a paper Wilhelmy plate under a continuous pressing speed for two barriers of 4.7 $mm \cdot min^{-1}$. Transfers were carried out by horizontal dipping at a surface pressure of 5 $mN \cdot m^{-1}$. The substrate was slowly approached to the surface at a speed of 0.2 $mm \cdot min^{-1}$ and raised at a speed of 10 $mm \cdot min^{-1}$. Then, it was submerged in water for 10 min and dried under a N_2 stream. This process was repeated for each transfer cycle. Experiments were carried out in a class 10 000 clean room at 22 °C and 50% humidity.

Physical Characterization. *UV−Visible Absorption Spectroscopy.* UV−vis absorption spectra were recorded on a Jasco V-670 spectrophotometer using transmission photometric mode.

Infrared reflection absorption spectra (IRRAS). Measurements were carried out on a VeeMax II sampling stage (Pike Technologies) placed in the sample compartment of a Nicolet 5700 Transformation-Infrared Spectrometer. All measurements were carried out under N_2 atmosphere. Each FT-IR spectrum represents the average of 512 scans at 4 cm^{-1} resolution. The infrared beam (incidence angle: 75°) was p-polarized by mean of a manual ZnSe polarizer, and the output signal was collected using a refrigerated mercury cadmium telluride detector.

Atomic force microscopy (AFM). Measurements were carried out with a Digital Instrument Veeco Nanoscope IVa microscope in tapping mode using silicon tips with natural resonance frequency of 300 kHz and with an equivalent constant force of 40 N m^{-1}.

Dynamic water CA. Measurements were carried out using a Ramé-hart Model 200 Standard Goniometer with Dropimage Standard v2.3 equipped with an automated dispensing system. The initial drop volume was 0.17 μL, increased by additions of 0.08 μL and waiting times of 1500 ms for each step.

X-ray Photoelectron Spectroscopy. X-ray photoelectron spectroscopy (XPS) was carried out ex situ at the X-ray Spectroscopy Service at the Universidad de Alicante using a Kα X-ray photoelectron spectrometer system (Thermo Scientific). All spectra were collected using Al Kα radiation (1486.6 eV) and monochromatized by a twin-crystal monochromator, yielding a focused X-ray spot (elliptical in shape with a major axis length of 400 μm) at 3 mA·C and 12 kV. The alpha hemispherical analyzer was operated in the constant energy mode with survey scan pass energies of 200 eV to measure the whole energy band and 50 eV in a narrow scan to selectively measure the particular elements. XPS data were analyzed with Avantage software. A smart background function was used to approximate the experimental backgrounds. Charge compensation was achieved with the system flood gun that provides low-energy electrons and low-energy argon ions from a single source. Spectra are referenced using the C 1s main peak (284.8 eV).

Matrix-Assisted Laser Desorption Ionization Time-of-Flight Mass Spectrometry. Samples were prepared as follows: α-Cyano-4-hydroxycinnamic acid (CHCA) matrix (1 μL of 5 $mg \cdot mL^{-1}$ CHCA (Bruker) in 0.1% TFA-ACN/H_2O (7:3, v/v)) was directly spotted onto the substrates to analyze and allowed to dry in air at room temperature. The samples were analyzed in a 5800 matrix-assisted laser desorption ionization time-of-flight (MALDI-TOF) instrument (ABSciex) in positive reflectron mode (3000 shots every position) in a mass range of 150−3000 m/z. Previously, the plate and the acquisition method were calibrated with a CalMix solution. The analysis was carried out at the Proteomics Unit in the central service for support of experimental investigation (servei central de suport a la investigació experimental, SCSIE) of the Universitat de València.

Grazing Incidence X-ray Diffraction. Thin films were measured at the I711 beamline of Max II (MAX IV Laboratory, Lund, Sweden), with a wavelength of λ = 0.9941 Å and a beam size of 200 × 200 μm^2, using a Newport diffractometer equipped with a Pilatus 100 K area detector mounted 76.5 cm from the sample. The detector was scanned continuously from 0 to 60° recording 125 images/° (step size 0.008°) for each measurement. The true 2θ position of each pixel was recalculated, yielding an average number of 100 000 pixels contributing to each 2θ value. Reflectivity as well as the diffraction signal were measured. Two different type of scans were carried out in all the cases: (a) symmetric scans ($\theta/2\theta$ scans), to detect the diffraction of the epitaxially grown layers, and (b) out-of-plane (2θ scans) above the critical angle, to detect disordered domains deposited over the substrate.

Electrical Characterization Resistance-Area (RA). Histograms were obtained from the analysis of the current (I) as a function of the applied bias (V, mercury-drop-biased positively) curves recorded after bringing a liquid-metal mercury drop into contact with the surface of the NAFS-1 surface and using the Py-C12P film as the bottom electrode. The area of the contact was estimated from the diameter of the contact zone measured using a CCD camera. Data was recorded using a Keithley 6517a electrometer controlled with Labview (National Instruments). Mercury drops with drop radius 0.035 cm were reproducibly produced using a WK2 hanging mercury drop electrode (IChF). See the Supporting Information for more details.

Brewster Angle Microscopy. Experiments carried out in a KSV NIMA 702BAM PTFE Langmuir trough (72 000 mm^2) equipped with an EP^3 Brewster angle microscope (Nanofilm Technologies). The floating films were prepared as described above. The laser wavelength was 532 nm. The incidence angle of the laser light was adjusted to 53.12° with respect to the surface normal. Images of the films at the air/liquid interface were captured by a CCD camera. Experiments were carried out in a class 10 000 clean room at 22 °C and 50% humidity.

RESULTS AND DISCUSSION

Directing MOF Transfer with Self-Assembled-Monolayers. NAFS-1 films were prepared according to the reported methodology with some modifications.[17] Freshly prepared chloroform/methanol solutions of CoTCPP and pyridine were dispersed onto aqueous solutions of copper(II) nitrate. Compression in the LB trough induces the formation of MOF 2D nanosheets that can be then transferred to the substrate of choice by horizontal dipping (Figure 1b). We encountered solubility problems when using the reported CoTCPP concentration of 0.2 mM. This required higher dilution (0.04 mM) and reoptimization of the procedure by evaluating the influence of the concentration of Cu(II) in the subphase and the salt counter ion in the formation of MOF nanodomains. Increasing the concentration from 1 to 100 mM or replacement of $Cu(NO_3)_2$ with $CuCl_2$ resulted in negligible changes on the pressure−area curves (Figures SI1 and SI2). The dynamic reorganization of the floating nanosheets formed in the air−liquid interface upon compression was studied with Brewster angle microscopy (BAM) in the range 0−25 $mN \cdot m^{-1}$ (Figure SI3). Snapshots of the Cu(II) subphase after addition of the CoTCPP-py solution and before compression confirm the presence of floating nanosheets that move randomly at high speed. As pressure increases, their movement is slowed down, and they start covering the surface of the subphase more homogeneously to finally form a continuous film. This evolution is consistent with that reported for the related NAFS-21.[18]

After defining the best-suited compression parameters, we proceeded with the fabrication of solid-supported MOF multilayered films by sequential transfer of the floating compressed layers to the substrate. MOF films were transferred onto bare Au, Si, and Py by vertical or horizontal dipping at variable dipping speeds. Transfer of NAFS-1 and related films to conventional substrates such as silicon and gold has been

DOI: 10.1021/jacs.5b09784
J. Am. Chem. Soc. 2016, 138, 2576−2584

reported,[19] but their nanostructuring onto ferromagnetic substrates remains unprecedented. We used permalloy (Py), a ferromagnetic nickel−iron alloy that develops a thin native oxide layer when exposed to air and thus protects the bulk from further oxidation. According to our results, although Si led to poor coverage and inhomogeneous distribution of patches across the substrate, transfer was not observed for bare Au and Py (Figure SI4). This is likely due to negligible interaction between the floating film and the bare substrate. Hence, we investigated the use of SAMs to modify the chemical nature of the substrate surface in order to direct the transfer. In line with our recent report on the use of the native oxide layer in Py as binding layer for the formation of *n*-alkylphosphonic acid SAMs,[20] we prepared Py-C12P by soaking plasma-cleaned Py substrates in isopropanolic solutions of 1-dodecylphosphonic acid (C12P). Unlike with unmodified Py, NAFS-1 nanosheets can be efficiently transferred to Py-C12P as confirmed by UV−vis (Figure 3a), AFM (Figure 4a), and MALDI-TOF mass spectrometry (Figure SI5). CA measurements suggest that the change in hydrophobicity after surface functionalization is key to favoring the transfer as surface CA changes from very hydrophilic (<20°) to hydrophobic (>100°). Similar alkyl SAM surface functionalizations have proven very efficient in assisting the growth of molecular films by modification of the substrate wettability.[21] To further prove the ability of SAMs to direct the transfer of NAFS-1 on other substrates, we used a glass substrate with 500 nm wide Au strips fabricated with a shadow mask. These last were selectively derivatized with C12S. AFM of the substrate after dipping in the LB trough (Figure 2) confirms the preferential deposition of NAFS-1 over the Au-C12S stripes, which display very homogeneous coverage, whereas unmodified glass is poorly covered by segregated patches.

MOF Thin Films on Ferromagnetic Permalloy. Multilayer thin films (up to 10 layers) of NAFS-1 over ferromagnetic Py-C12P were fabricated by sequential LbL growth cycles by following three steps: transfer of the floating MOF nanosheets to the substrate (horizontal geometry), rinsing with water, and drying with N_2. Transfer was found to be more consistent when the substrate approach was extremely slow in the advancing and very fast in the receding step. Sequential transfer of the material was first evaluated by studying the evolution of the UV−vis absorption of the films (Figure 3a). Spectra are dominated by an intense Soret peak at 438 nm, characteristic of porphyrin units. This band is slightly red-shifted with respect to CoTCPP as result of Cu(II) coordination. Maxima absorbance displays a linear increase with the number of transfer cycles confirming that the same amount of material is transferred in each cycle. Although our results are consistent with the growth of NAFS-1 on quartz,[18] deposition of uncoordinated CoTCPP units might lead to similar results with minor changes linked to metal coordination.

Sequential growth was additionally confirmed with infrared reflectance absorption spectroscopy (IRRAS, Figure 3b). Metal complexation, indicative of NAFS-1 formation, is confirmed by the presence of asymmetric (asym) and symmetric (sym) stretching modes of the $-COO^-$ group at 1624 and 1404 cm^{-1}.[22] These modes are accompanied by a weaker absorption at 1710 cm^{-1} that can be attributed to the C═O stretching mode from a very small fraction of free −COOH groups present in the films. To rule out simple coprecipitation of CoTCPP with Cu(II) in our films, we analyzed the IR of bulk CoTCPP. The appearance of a strong, broad band close to

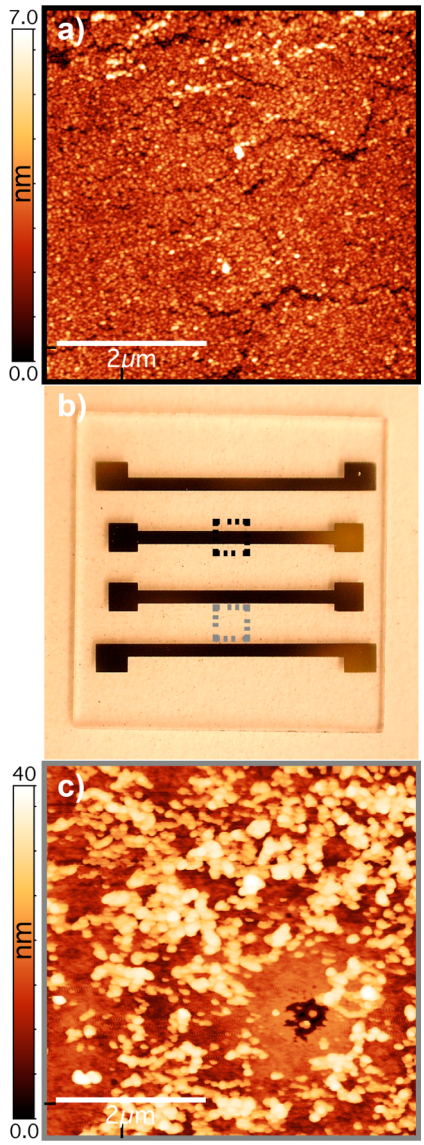

Figure 2. Preferential deposition of NAFS-1 on SAM-functionalized Au stripes on a glass substrate. (a) AFM topographic image of 1 transfer on the Au-C12S area (black dashed square in b); the coverage is good with few empty gaps. (b) Picture of glass substrate with 500 μm wide Au strips fabricated with a shadow mask. (c) AFM topography image of a single transfer on the unmodified glass area (gray dashed square in b) showing very poor transfer with low coverage and unevenly distributed patches of material.

1700 cm^{-1}, linked to C═O stretching mode of free −COOH groups, is indicative of the presence of uncoordinated CoTCPP units (Figure SI7). This signal is merely residual in our films, suggesting that free −COOH groups reside exclusively at the edges of the film. To confirm that the absence of this signal accounts for the formation of coordination polymers based on binuclear paddle wheel copper units also present in NAFS-1, we next analyzed a tetracarboxylate porphyrin MOF (PPF-3), prepared by solvothermal reaction of 5,10,15,20-tetrakis(4-carboxyl)-21H,23H-porphine, $Co(NO_3)_2$, and bipyridine[23] and the solid that results from addition of CoTCPP and pyridine dissolved in CH_3OH:$CHCl_3$ mixtures to an aqueous solution of $Cu(NO_3)_2$. As shown in Figure SI7, FT-IR spectra confirms that the band centered at 1700 cm^{-1} disappears, in both cases giving rise to the appearance of bands at 1625 and 1400 cm^{-1},

DOI: 10.1021/jacs.5b09784
J. Am. Chem. Soc. 2016, 138, 2576−2584

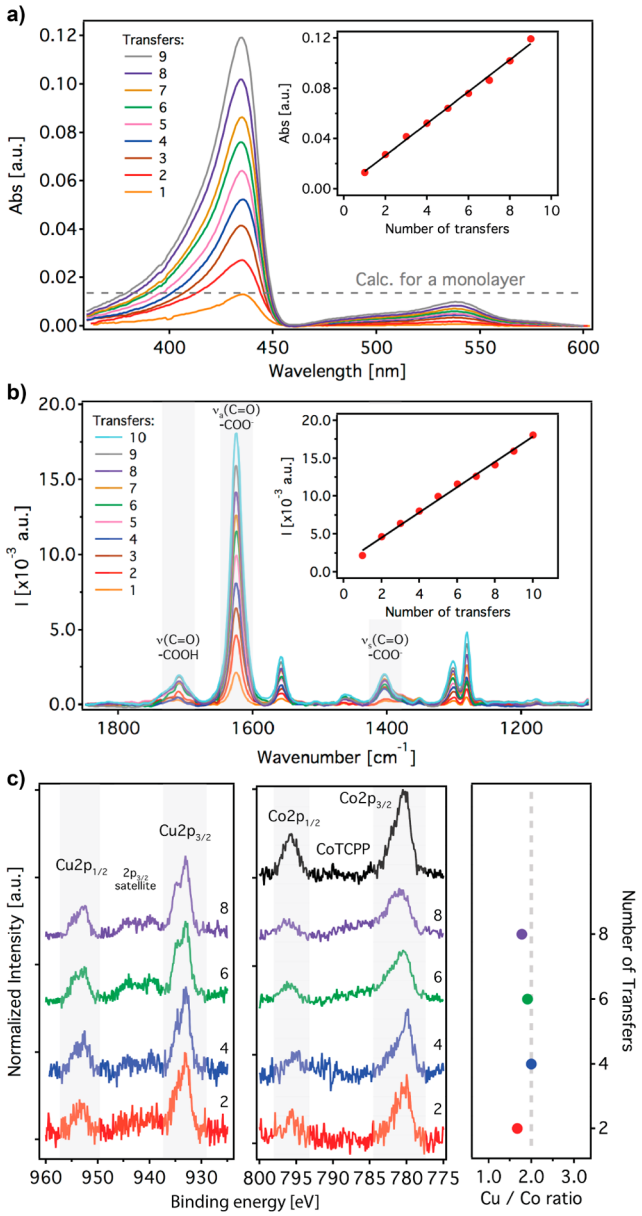

Figure 3. Characterization of NAFS-1 thin films as a function of the number of transfers. (a) UV−vis absorption spectra after successive transfer cycles. Dashed light blue line stands for the theoretical maximum absorbance of the Soret band for a NAFS-1 monolayer. The inset shows the maximum absorbance of the Soret band against the number of transfers. Data have been fitted to a linear regime (black line). (b) IRRAS spectra after successive growth cycles. The inset shows the maximum absorbance of the most intense peak, $\nu(COO_{asym})$ at 1620 cm^{-1}, against the number of transfers. Data have been fitted to a linear model (black line). (c) High-resolution XPS spectra for a set of films and the reference CoTCPP complex showing the Cu 2p and Co 2p regions. The Cu/Co ratio remains almost constant and is consistent with the theoretical value (dashed gray line) for all transfers.

which can be associated with asymmetric and symmetric stretching modes of the carboxylate group that become active with the formation of CoTCPP-Cu units. For films growth onto metallic surfaces, IRRAS is very sensitive to the orientation and quality of the film: Signals coming from vibrations parallel to the surface are enhanced, whereas those coming from vibrations normal to the surface are reduced.[24] The marked difference between the asym and sym contributions in our films indicates that the $-COO^-$ asym vibration are mainly parallel to the surface confirming the flat planar orientation of the tetracarboxylate porphyrin units, and thus the MOF layer, with respect to the surface. This fact is consistent with the selection rules that apply to IRRAS onto metallic surfaces and confirms the good quality of our films. Even more, this difference in intensity scales up with the number of transfers so that the orientation is maintained for multilayer deposition. IRRAS is representative of all the film rather than segregated domains, so we believe this is an unambiguous indication of the formation of a highly oriented film across a millimeter-scale area. To further confirm the direct relationship between asym/sym intensity ratio with the orientation of the film, we prepared NAFS-1 films according to the described methodology but used a highly corrugated substrate by evaporating Py over unpolished glass. As shown in Figure SI8, IRRAS of this film displays asym and sym $-COO^-$ modes with an intensity ratio closer to that featured by the bulk formed by direct reaction of CoTCPP, pyridine, and Cu-$(NO_3)_2$. This accounts for the formation of a poorly oriented film with random orientation of carboxylate groups. Previous reports for the deposition of NAFS-2 on bare Au confirm that the observed difference in intensities is consistent with preferential orientation of MOF layers.[19a] A similar analysis has been recently used by Terfort and co-workers to study the formation of oriented $[Cu_2(F_4bdc)_2(dabco)]$ SURMOFs featuring equivalent Cu_2 paddle wheel units.[25]

X-ray photoelectron spectroscopy (XPS) analysis for a set of representative samples (2, 4, 6, and 8 transfers) confirms the presence of Co and Cu in the Py-C12P/NAFS-1 films with binding energies (BEs) in agreement with those of the expected bonding states (Figure 3c). BE values extracted from high-resolution spectra are summarized in Table SI1. For all transfers, high-resolution Co 2p spectra display a dominant Co($2p_{3/2}$) peak centered at 780.3 eV and a weaker Co($2p_{1/2}$) signal at 795.8 eV. The shape of the peaks and BE values are very close to those of bulk CoTCPP, used as reference, supporting the presence of Co(II) units in the films. As for the high-resolution Cu 2p spectra, it displays a similar profile with an asymmetric doublet that splits into Cu($2p_{3/2}$) and Cu($2p_{1/2}$) peaks at around 933.1 and 952.8 eV. The Cu($2p_{3/2}$) level is accompanied by a less intense shakeup satellite peak at higher binding energies that confirms the presence of Cu(II) species.[26] The overall amount of Co and Cu species in the films was quantified from integration of their peak areas. The average Cu/Co ratio of 1.84 ± 0.15 agrees well with the theoretical 2:1 value and is consistent with the formation of a homogeneous CoTCPP-py-Cu multilayered array for the number of transfers explored.

AFM was used to correlate the number of transfer cycles with the thickness and surface morphology of the films. Figure 4a−c displays topographic images (5 μm × 5 μm) of Py-C12P/NAFS-1 films after 1, 5, and 10 transfers. A single transfer results in a partially covered, rough surface with visible gaps. In line with BAM measurements (described above), this is consistent with the transfer of a discontinuous film built from the compression of NAFS-1 2D nanosheets in the LB trough, which is far from ideal and leaves nanometric gaps. Transfer of additional layers results in the formation of continuous films. Surface coverage can be also correlated with changes on the wetting properties of the surface of the substrate. Dynamic CA measurements indicate that the hydrophobicity of the original

DOI: 10.1021/jacs.5b09784
J. Am. Chem. Soc. 2016, 138, 2576−2584

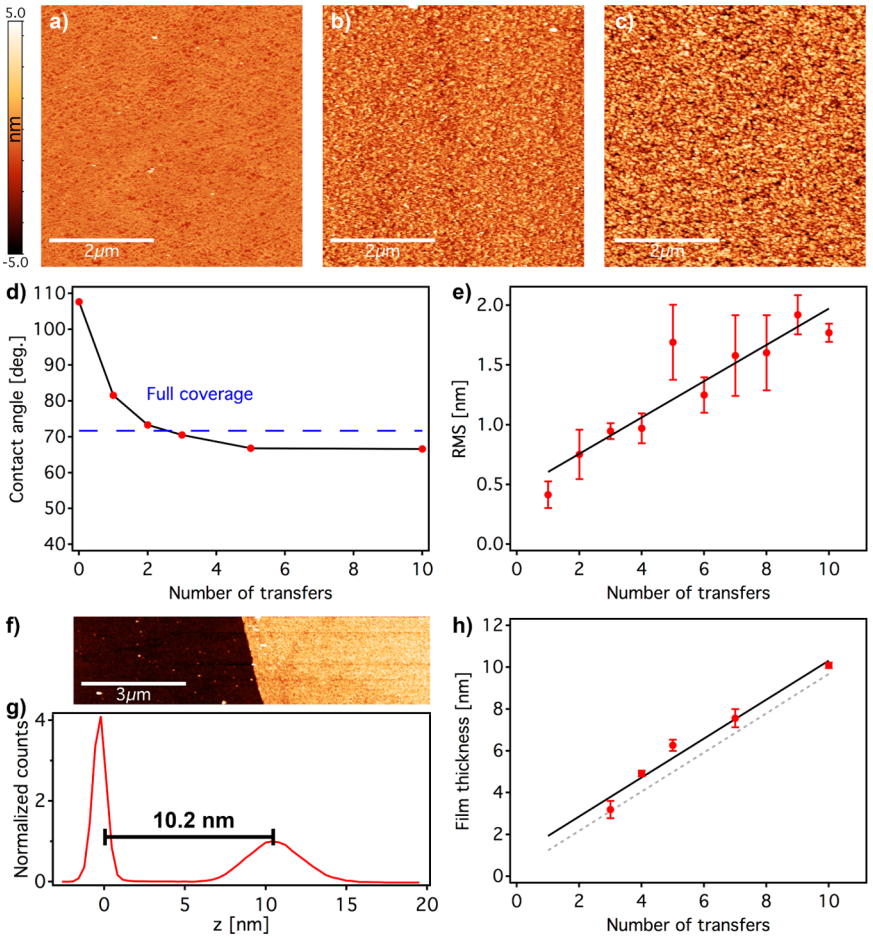

Figure 4. Surface analysis of NAFS-1 multilayer thin films deposited on Py-C12P. AFM topography images of (a–c) 1, 5, and 10 transfers show the progressive increase in coverage and roughness of the films. Although some gaps revealing the underlying Py-C12P substrate are present in the 1-transfer image (a), these are not present for the 5- and 10-transfer images (b and c). (d) Evolution of the contact angle (CA) of the films with the number of transfers that reaches a stable value (blue dashed line) right after two transfers. This suggests the formation of smooth, homogeneous films from this point on. (e) RMS roughness versus the number of transfers showing a steady increase in roughness from ∼0.4 nm to ∼1.9 nm after 10 transfers. Data have been fitted to a linear model (black line). (f) AFM topographic image of a manually scratched 10-transfer film, image resolution is 512 × 128. (g) Height distribution of the above image showing a thickness value of 10.2 nm. (h) Evolution of film thickness with the number of transfers. Height distributions were extracted from AFM images of manually scratched samples with a resolution of 512 × 128. Experimental thickness values were calculated by averaging at least two samples. Data fit confirms sequential deposition of a single cell of NAFS-1 with average thickness of 0.93 nm (blue line), consistent with the proposed structural model (black line).[17]

Py-C12P surface is progressively reduced by MOF deposition as the CA decreases from the original value of 107° down to a minimum of 66° (Figure 4d). This decrease is very sharp for the initial steps and becomes quite stable after two or three transfers, suggesting that full surface coverage is reached from that point on. To confirm the sequential growth of the MOF architecture, we also monitored the correlation between the thickness and roughness of the films with the number of transfers. As shown in Figure 4f,g, we manually scratched away the film from the substrate with a toothpick to produce sharp steps and analyzed the height difference between bare and coated areas in five different regions along the step for at least two samples to obtain more reliable measurements. See Figure SI5 for height distributions for all samples. Only small height variations (<0.6 nm) were measured along the edge, confirming the homogeneity of the film. Thickness of NAFS-1 films increases linearly with the number of transfers (Figure 4h). The structural model first proposed by Kitagawa et al. estimates a length of 0.938 nm for the *c* axis (preferential growth direction) of NAFS-1 by assuming that the neighboring CoTCPP-py-Cu are interdigitated by $\pi-\pi$ stacking.[18] Our data reveals that each transfer cycle corresponds to the deposition of a single layer with an average thickness of 0.93 ± 0.09 nm which is quite close to that of a single cell of NAFS-1. Surface root-mean-square (RMS) roughness, estimated from topographic AFM 1 μm × 1 μm images, also follows a linear trend with the number of transfers up to 10 cycles. Roughness scales from 0.4 to 1.9 nm, which corresponds to a maximum step height of approximately two unit cells (Figure 4e). Overall, this rules out the formation of segregated domains and confirms the formation of very smooth, homogeneous, ultrathin films of NAFS-1 across millimetric areas. This is a key requirement for the integration of MOFs as active interfaces in electronic devices because the quality of the interface is expected to modulate the electronic communication between components in the assembled heterostructure, thus controlling the overall performance of the device.[27]

We also used synchrotron radiation for studying the layered structure of the films with grazing incidence X-ray diffraction (GIXRD). The reflectivity and diffraction ($\theta/2\theta$ configuration)

DOI: 10.1021/jacs.5b09784
J. Am. Chem. Soc. 2016, 138, 2576–2584

of Py-C12P/NAFS-1 (10 transfers) thin films are dominated by the presence of the 15 nm thick permalloy layer used to template the assembly of NAFS-1 (Figure SI9). Fit of the reflectivity accounts for the presence of a 15 nm thick layer of Py, whereas indexing of the diffraction pattern is consistent with the presence of metallic Ni (cubic $Fm\bar{3}m$; a = 3.529 ± 0.001 Å) from Py. Absence of NAFS-1 diffraction is likely linked to the higher electronic density of Py (alloy of metallic Ni an Fe) and the ultrathin nature of the MOF film under study (only 10 nm), suggesting that Py is not an adequate substrate for studying ultrathin MOF film formation by GIXRD. This can be more easily attained by using nonmetallic substrates like silicon or SiO_2, as previously demonstrated by Kitagawa and co-workers for 20 nm thick NAFS-1 films.[17]

Effect of Thickness over Charge Transport in MOF Ultrathin Films (<10 nm). Electrical properties of NAFS-1 films were studied with the hanging-mercury-drop electrode technique that makes use of the micrometer-scale junctions formed from bringing together a small liquid-metal mercury drop and the surface of the film. Hence, electrical characteristics of the film can be determined by measuring the current (I) flowing between the top electrode (mercury drop) and the bottom electrode (Py-C12P substrate in our case) as a function of the applied bias (V). Additional imaging equipment is used to measure the contact area with high precision in order to confirm the expected scaling of the measured current with the contact area. In contrast with other contacting techniques, this is especially well-suited to study ultrathin films of soft materials with nanometer-scale thicknesses because the liquid nature of the top electrode allows for directly contacting the sample with no damage.[28] Hg-drop electrodes have been used to characterize aliphatic and aromatic SAMs[29] or metal complexes,[30] but to the best of our knowledge, they have never been used for studying the electrical properties of as-grown MOF films. Even more, unlike more conventional techniques such as the van der Pauw method,[31] this experimental configuration relies on the vertical transport of charge carriers between electrodes through nanometer-scale thick films. This scenario is much closer to transport phenomena in spintronic and optoelectronic devices and also allows for evaluating the effect of the film thickness over the overall conductance.

Current−voltage characteristics of Py-C12P and NAFS-1 films after 2, 4, 6, 7, and 8 transfers were analyzed by averaging hundreds of I−V curves measured for multiple Hg-drop contacts at different positions across the surface of each film. Current density (J) curves display the expected V-shape for a nonmetallic contact and scale down for increasing film thickness (Figure 5a). They show a small current asymmetry (As) independent of the film thickness (As = $|J(-0.2\ \mathrm{V})|/|J(+0.2\ \mathrm{V})| \cdot 100 \approx 85 \pm 6\%$; mercury-drop-biased positively) that is probably reflecting the dissimilarity between Hg and Py-C12P electrodes. To evaluate the change in resistance with the thickness of the film (Supporting Information) we calculated the product of resistance and area (RA) at ±0.1 V from each I−V curve as a function of the number of transfers. As shown in Figure 5b, our statistical analysis results in a log-normally distributed variation in the product RA for the initial Py-C12P substrate and Py-C12P/NAFS-1 films after 2, 4, 6, 7, and 8 transfers, which is consistent with physically meaningful data ruling out experimental artifacts.[32] To draw conclusions on the transport mechanism, we fitted our data to the equation below:

$$RA = RA_0\, e^{(\beta d)} \qquad (1)$$

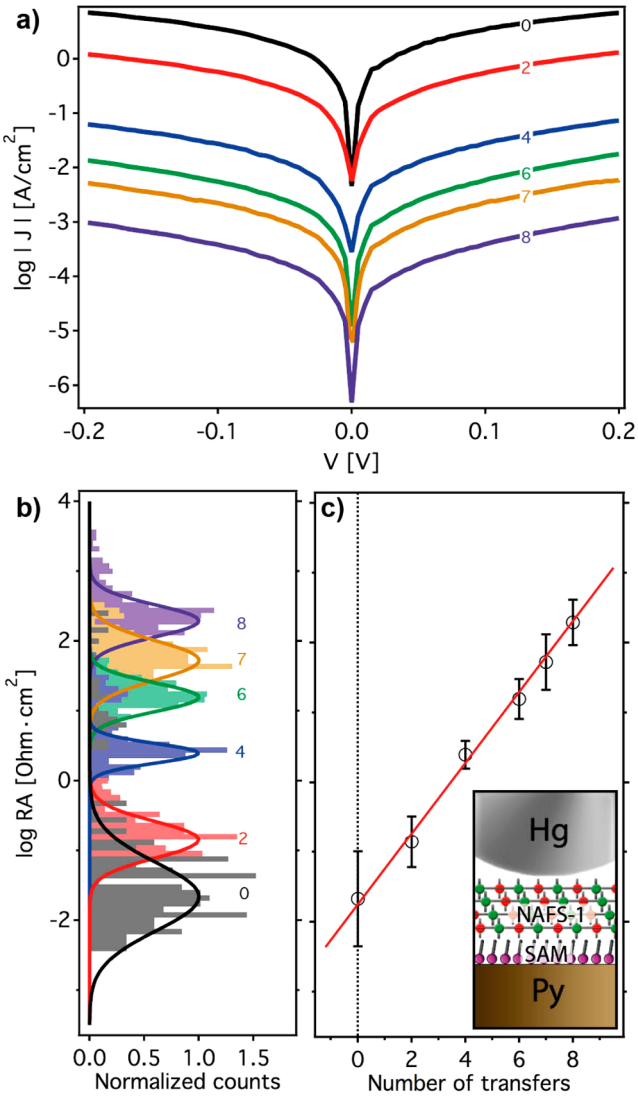

Figure 5. Electrical characterization of NAFS-1 films. (a) NAFS-1 current density ($J = I/A$) curves as a function of the applied voltage and the number of transfers. Curves are the average of more than 100 traces measured at different positions over the surface of each film. (b) Dependence of the resistance−area (RA) product as a function of the number of transfers. (c) Average RA value as a function of the number of transfers. Error bars correspond to the Gaussian width. The straight red line is a linear fit to the data according to $\log RA = \log (RA)_0 + \beta(\text{Number of layers})/2.303$, where β = 1.17 ± 0.14 transfer^{-1} = 0.12 Å^{-1}. (According to AFM data, one transfer corresponds to 9.3 Å.)

where β is the attenuation factor intrinsic to the electronic properties of the film, d stands for its thickness, and RA_0 is a factor that accounts for the interfaces between the film and the electrodes. According to previous works on SAM-based junctions and molecular wires, high β values (>0.1 Å^{-1}) are characteristic of electronic transport in the tunnelling regime (strong dependence of the resistance with the film thickness), whereas much lower values (<0.1 Å^{-1}) are instead characteristic of hopping (weak dependence). Transition from direct tunnelling to hopping (β < ca. 0.1 Å^{-1}) has been also observed for conjugated molecular wires when going from short (d < 3−4 nm) to longer wires.[33] In our case, variation of the log RA product with the number of transfers can be fitted to a single straight line (Figure 5c) with a quite low β of 0.12 Å^{-1}. This rules out transition between transport mechanisms, in good

DOI: 10.1021/jacs.5b09784
J. Am. Chem. Soc. 2016, 138, 2576−2584

agreement with that reported for other coordination complexes,[30a,34] and suggests that hopping dominates charge transport through NAFS-1 films for the thickness range analyzed (d < 10 nm). Even more, tunnelling probability is expected to decay exponentially with the distance separating the electrodes. Hence, tunnelling through distances as long as 9 nm is quite unlikely, and charge transfer by electron-/hole-hoping between redox active metal sites distributed across the MOF layers seems the most plausible transport mechanism. Our findings are consistent with recent electrochemical studies carried out on micrometer-scale thick films of the related metalloporphyrin MOF CoPIZA that supports the idea of a redox-hopping mechanism being responsible for the charge transport.[35]

In the last year, reasonably high electrical conductivities have been reported for micrometer-scale thick MOF films. Allendorf et al. reported conductivities up to 7 S m^{-1} in 100 nm thick films of 3D HKUST-1 ($Cu_3(btc)_2$; btc = benzene-1,3,5-tricarboxylic acid) by infiltrating redox-active 7,7,8,8-tetracyanoquinododimethane (TCNQ) molecules.[36] Intrinsic conductivity of 20 S·m^{-1} at room temperature has been more recently reported for bulk pellets of the 2D MOF $Cu_3(HITP)_2$ (HITP = 2,3,6,7,10,11-hexaiminotriphenylene).[37] This likely arises from the electronic interaction between metal nodes and the charge delocalized by extensive π conjugation across MOF layers. These examples confirm that the unparalleled synthetic/structural flexibility of MOFs allows for overcoming their generally accepted insulating character. The development of MOF-based electronic devices is somewhat more limited by their processing as nanometer-scale thin films with exquisite control over smoothness, thickness, and orientation rather than their intrinsic electrical conductivity.

CONCLUSIONS

Our approach enables fabrication of high-quality ultrathin films of NAFS-1 by utilizing SAMs of C12P that direct the transfer of 2D MOF nanosheets from solution and allow for preferential deposition parallel to the surface regardless the substrate. SAM-assisted transfer is also used for transferring NAFS-1 onto a nonconventional, ferromagnetic substrate such as Py. Next, Hg-drop micrometric electrode junctions were used to study vertical charge transport in Py-C12P/NAFS-1 films (<10 nm) and evaluate the effect of the thickness of the MOF interface over the conductance. Our results indicate that hopping is the most likely mechanism for charge transport in NAFS-1. This strategy might be useful for the integration of MOFs as active interfaces in hybrid (spin) electronic devices. This unprecedented application of nanostructured MOFs is chemically much more demanding than more conventional ones such as sensing, gas storage, or catalysis because it requires the organization of continuous, high-quality, ultrathin films (below 10 nm) of these materials on surfaces. Still, the accomplishment of this critical and challenging step can open new perspectives in the use of MOFs in molecular (spin) electronics. Here, the transport of charge carriers as well as the spin injection across this MOF interface could be manipulated by loading of molecular guests in the porous scaffold. In addition, the open structures of these crystalline materials display higher surface areas for direct contact with the molecules than those offered by a normal 2D surface. These complex hybrid interfaces, integrated by an open framework and molecular guests, are linked to a new idea of assembled 3D interfaces with addressable functionality, which may generate conceptually new hybrid devices. In this line, the possibility of incorporating molecules with different functionalities (magnetism, bistability, luminescence, etc.) or increasing the intrinsic conductivity of the framework could enlarge the versatility of these complex interfaces.

ASSOCIATED CONTENT

Supporting Information

The Supporting Information is available free of charge on the ACS Publications website at DOI: 10.1021/jacs.5b09784.

Figure SI1−SI15, Table SI1, and further details on the electrical characterization of the films. (PDF)

AUTHOR INFORMATION

Corresponding Authors

*E-mail: carlos.marti@uv.es.

*E-mail: eugenio.coronado@uv.es.

Present Address

F.V.: Université Pierre et Marie Curie Paris 6,4 Place Jussieu, 75252, Paris, France.

Notes

The authors declare no competing financial interest.

ACKNOWLEDGMENTS

Financial support from the EU (ERC Advanced Grant SPINMOL and FP7/2012-321739 SAMSFERE), the Spanish MINECO (Project MAT-2014-56143-R and Unidad de Excelencia María de Maeztu MDM-2015-0538), the Generalitat Valenciana (Prometeo) and the Universitat de València (PRECOMP14-202646). V.R.-G thanks the Spanish MECD for a FPU predoctoral grant; S.T. and C.M.-G. thank the Spanish MINECO for a Juan de la Cierva and Ramón y Cajal Fellowships. We are also grateful to Carlos Rubio-Giménez for the pictures illustrating Figure 1 and 5c, to Ángel López-Muñoz, Eva Tormos, and Michele Mattera for their technical support, and to Efrén Navarro-Moratalla and Guillermo Mínguez-Espallargas for helpful discussions.

REFERENCES

(1) Han, C.; Park, J.; Choi, H.; Kim, T.; Shin, Y.; Shin, H.; Lim, M.; Kim, B.; Kim, H.; Kim, B.; Tak, Y.; Oh, C.; Cha, S.; Ahn, B. *J. Soc. Inf. Disp.* **2014**, *22*, 552−563.

(2) Gratzel, M. *Nat. Mater.* **2014**, *13*, 838−842.

(3) Sessolo, M.; Bolink, H. J. *Adv. Mater.* **2011**, *23*, 1829−1845.

(4) Galbiati, M.; Tatay, S.; Barraud, C.; Dediu, A. V.; Petroff, F.; Mattana, R.; Seneor, P. *MRS Bull.* **2014**, *39*, 602−607.

(5) (a) Sanvito, S. *Nat. Phys.* **2010**, *6*, 562−564. (b) Dediu, V. A. *Nat. Phys.* **2013**, *9*, 210−211.

(6) (a) Barraud, C.; Seneor, P.; Mattana, R.; Fusil, S.; Bouzehouane, K.; Deranlot, C.; Graziosi, P.; Hueso, L.; Bergenti, I.; Dediu, V.; Petroff, F.; Fert, A. *Nat. Phys.* **2010**, *6*, 615−620. (b) Raman, K. V.; Kamerbeek, A. M.; Mukherjee, A.; Atodiresei, N.; Sen, T. K.; Lazic, P.; Caciuc, V.; Michel, R.; Stalke, D.; Mandal, S. K.; Blugel, S.; Munzenberg, M.; Moodera, J. S. *Nature* **2013**, *493*, 509−513.

(7) MacGillivray, L. R.; Lukehart, C. M. *Metal−Organic Framework Materials*; Wiley: West Sussex, U.K., 2014.

(8) (a) Suh, M. P.; Park, H. J.; Prasad, T. K.; Lim, D. *Chem. Rev.* **2012**, *112*, 782−835. (b) Sumida, K.; Rogow, D. L.; Mason, J. A.; McDonald, T. M.; Bloch, E. D.; Herm, Z. R.; Bae, T. H.; Long, J. R. *Chem. Rev.* **2012**, *112*, 724−781. (c) Chae, H. K.; Siberio-Perez, D. Y.; Kim, J.; Go, Y.; Eddaoudi, M.; Matzger, A. J.; O'Keeffe, M.; Yaghi, O. M. *Nature* **2004**, *427*, 523−527.

(9) (a) Bloch, E. D.; Queen, W. L.; Krishna, R.; Zadrozny, J. M.; Brown, C. M.; Long, J. R. *Science* **2012**, *335*, 1606−1610. (b) Li, J. R.; Sculley, J.; Zhou, H. C. *Chem. Rev.* **2012**, *112*, 869−932.

DOI: 10.1021/jacs.5b09784
J. Am. Chem. Soc. 2016, 138, 2576−2584

(10) (a) Wee, L. H.; Alaerts, L.; Martens, J. A.; De Vos, D. In *Metal–Organic Frameworks as Catalysts for Organic Reactions in Metal-Organic Frameworks: Applications from Catalysis to Gas Storage*; Farrusseng, D., Ed.; Wiley-VCH Verlag GmbH & Co. KGaA: Weinheim, Germany, 2011. (b) Corma, A.; Garcia, H.; Llabres i Xamena, F. X. *Chem. Rev.* **2010**, *110*, 4606–4655. (c) Zhang, T.; Lin, W. *Chem. Soc. Rev.* **2014**, *43*, 5982–5993.
(11) (a) Kreno, L. E.; Leong, K.; Farha, O. K.; Allendorf, M.; Van Duyne, R. P.; Hupp, J. T. *Chem. Rev.* **2012**, *112*, 1105–1125. (b) Chen, B.; Wang, L.; Xiao, Y.; Fronczek, F. R.; Xue, M.; Cui, Y.; Qian, G. A. *Angew. Chem., Int. Ed.* **2009**, *48*, 500–503.
(12) (a) Horike, S.; Umeyama, D.; Kitagawa, S. *Acc. Chem. Res.* **2013**, *46*, 2376–2384. (b) Yoon, M.; Suh, K.; Natarajan, S.; Kim, K. *Angew. Chem., Int. Ed.* **2013**, *52*, 2688–2700.
(13) (a) Betard, A.; Fischer, R. A. *Chem. Rev.* **2012**, *112*, 1055–1083. (b) Bradshaw, D.; Garai, A.; Huo, J. *Chem. Soc. Rev.* **2012**, *41*, 2344–2381. (c) Talham, D. R.; Meisel, M. W. *Chem. Soc. Rev.* **2011**, *40*, 3356–3365.
(14) Zacher, D.; Schmid, R.; Wöll, C.; Fischer, R. A. *Angew. Chem., Int. Ed.* **2011**, *50*, 176–199.
(15) Liu, B. *J. Mater. Chem.* **2012**, *22*, 10094–10101.
(16) Stavila, V.; Talin, A. A.; Allendorf, M. D. *Chem. Soc. Rev.* **2014**, *43*, 5994–6010.
(17) Makiura, R.; Motoyama, S.; Umemura, Y.; Yamanaka, H.; Sakata, O.; Kitagawa, H. *Nat. Mater.* **2010**, *9*, 565–571.
(18) Makiura, R.; Konovalov, O. *Dalton Trans.* **2013**, *42*, 15931–15936.
(19) (a) Motoyama, S.; Makiura, R.; Sakata, O.; Kitagawa, H. *J. Am. Chem. Soc.* **2011**, *133*, 5640–5643. (b) Xu, G.; Otsubo, K.; Yamada, T.; Sakaida, S.; Kitagawa, H. *J. Am. Chem. Soc.* **2013**, *135*, 7438–7441.
(20) Mattera, M.; Torres-Cavanillas, R.; Prieto-Ruiz, J. P.; Prima-García, H.; Tatay, S.; Forment-Aliaga, A.; Coronado, E. *Langmuir* **2015**, *31*, 5311–5318.
(21) (a) Liu, S.; Wang, W. M.; Mannsfeld, S. C. B.; Locklin, J.; Erk, P.; Gomez, M.; Richter, F.; Bao, Z. *Langmuir* **2007**, *23*, 7428–7432. (b) Kim, H.; Meihui, Z.; Battaglini, N.; Lang, P.; Horowitz, G. *Org. Electron.* **2013**, *14*, 2108–2113. (c) Walter, S. R.; Youn, J.; Emery, J. D.; Kewalramani, S.; Hennek, J. W.; Bedzyk, M. J.; Facchetti, A.; Marks, T. J.; Geiger, F. M. *J. Am. Chem. Soc.* **2012**, *134*, 11726–11733.
(22) Nakamoto, K. *Infrared and Raman Spectra of Inorganic and Coordination Compounds*; Wiley: New York, 1978.
(23) Choi, E.-Y.; Barron, P. M.; Novotny, R. W.; Son, H.-T.; Hu, C.; Choe, W. *Inorg. Chem.* **2009**, *48*, 426–428.
(24) Greenler, R. G. *J. Chem. Phys.* **1966**, *44*, 310–315.
(25) Zhuang, J.-L.; Kind, M.; Grytz, C. M.; Farr, F.; Diefenbach, M.; Tussupbayev, S.; Holthausen, M. C.; Terfort, A. *J. Am. Chem. Soc.* **2015**, *137*, 8237–8243.
(26) Poulston, S.; Parlett, P. M.; Stone, P.; Bowker, M. *Surf. Interface Anal.* **1996**, *24*, 811–820.
(27) Ma, H.; Yip, H.; Huang, F.; Jen, A. K. *Adv. Funct. Mater.* **2010**, *20*, 1371–1388.
(28) McCreery, R. L.; Bergren, A. J. *Adv. Mater.* **2009**, *21*, 4303–4322.
(29) Haick, H.; Cahen, D. *Prog. Surf. Sci.* **2008**, *83*, 217–261.
(30) (a) Tuccitto, N.; Ferri, V.; Cavazzini, M.; Quici, S.; Zhavnerko, G.; Licciardello, A.; Rampi, M. A. *Nat. Mater.* **2009**, *8*, 41–46. (b) Rampi, M. A.; Whitesides, G. M. *Chem. Phys.* **2002**, *281*, 373–391. (c) Holmlin, R. E.; Haag, R.; Chabinyc, M. L.; Ismagilov, R. F.; Cohen, A. E.; Terfort, A.; Rampi, M. A.; Whitesides, G. M. *J. Am. Chem. Soc.* **2001**, *123*, 5075–5085.
(31) van der Pauw, L. J. *Philips Technol. Rev.* **1958**, *20*, 220–224.
(32) (a) Reus, W. F.; Nijhuis, C. A.; Barber, J. R.; Thuo, M. M.; Tricard, S.; Whitesides, G. M. *J. Phys. Chem. C* **2012**, *116*, 6714–6733. (b) Yuan, L.; Jiang, L.; Zhang, B.; Nijhuis, C. A. *Angew. Chem., Int. Ed.* **2014**, *53*, 3377–3381.
(33) Ho Choi, S.; Kim, B.; Frisbie, C. D. *Science* **2008**, *320*, 1482–1486.
(34) (a) Musumeci, C.; Zappalà, G.; Martsinovich, N.; Orgiu, E.; Schuster, S.; Quici, S.; Zharnikov, M.; Troisi, A.; Licciardello, A.; Samorì, P. *Adv. Mater.* **2014**, *26*, 1688–1693. (b) Li, Z.; Park, T. H.; Rawson, J.; Therien, M. J.; Borguet, E. *Nano Lett.* **2012**, *12*, 2722–2727.
(35) Ahrenholtz, S. R.; Epley, C. C.; Morris, A. J. *J. Am. Chem. Soc.* **2014**, *136*, 2464–2472.
(36) Talin, A. A.; Centrone, A.; Ford, A. C.; Foster, M. E.; Stavila, V.; Haney, P.; Kinney, R. A.; Szalai, V.; El Gabaly, F.; Yoon, H. P.; Leonard, F.; Allendorf, M. D. *Science* **2014**, *343*, 66–69.
(37) Campbell, M. G.; Sheberla, D.; Liu, S. F.; Swager, T. M.; Dincă, M. *Angew. Chem., Int. Ed.* **2015**, *54*, 4349–4352.

DOI: 10.1021/jacs.5b09784
J. Am. Chem. Soc. 2016, 138, 2576–2584